

## Quantitative estimation of the underwater radiance distribution

Marlon R. Lewis,<sup>1,2</sup> Jianwei Wei,<sup>1</sup> Ronnie Van Dommelen,<sup>2</sup> and Kenneth J. Voss<sup>3</sup>

Received 5 May 2011; revised 5 July 2011; accepted 13 July 2011; published 15 October 2011.

[1] Within the Radiance in a Dynamic Ocean (RaDyO) program, we have created and deployed a high dynamic range camera that can resolve the full spherical radiance distribution at the ocean surface and at depth. We present here the first results from deployments of the camera in near-surface water in eutrophic, mesotrophic, and oligotrophic environments. The instrument resolves the dynamics and fine structure of both the downwelling and upwelling radiance distribution and its variation with depth in these optically diverse water types. The various irradiances ( $E_d$ ,  $E_u$ ,  $E_o$ ,  $E_{ou}$ , and  $E_{od}$ ) are computed by integration. The distribution functions (e.g., the average cosines) are computed directly, as are the various diffuse attenuation coefficients. The fully specified radiance field therefore provides all the pertinent information to derive not only all of the apparent optical properties but, in principle, the inherent optical properties such as the absorption coefficient and the phase function as well. Comparison of the measured radiance field to independent measurements has shown very good agreement.

**Citation:** Lewis, M. R., J. Wei, R. Van Dommelen, and K. J. Voss (2011), Quantitative estimation of the underwater radiance distribution, *J. Geophys. Res.*, 116, C00H06, doi:10.1029/2011JC007275.

### 1. Introduction

[2] A significant source of uncertainty in the prediction of the optical properties of the ocean is the geometrical distribution of the radiance field and its variation with respect to time and space; this uncertainty directly affects attempts to use measurements of reflectance and attenuation for the diagnosis of ocean constituents. Uncertainties in the time- and depth-dependent variations in the radiance distribution, and their sources of variation, propagate as well to the prediction of the performance of new imaging systems such as the “virtual periscope” [Hubbard *et al.*, 2006].

[3] The problem of predicting the radiance distribution starts at the sea surface, where the sky radiance distribution is generally unknown and the wind-roughened air-sea interface causes variability in the transmission of sun and sky radiance to below the surface. In the ocean interior, the volume scattering function and the absorption coefficient alter the radiance distribution in both the forward and backward direction; with multiple scattering and internal sources such as fluorescence and Raman scattering, the uncertainty in the radiance distribution becomes large. In optically shallow areas, non-Lambertian bottom reflectances add to the problem.

[4] Several models have been put forward for the variation in the upwelling radiance field and the effect of this variation on interpretation of measurements of the ocean

reflectance made above the water [e.g., Mobley, 1989; Morel and Gentili, 1993; Voss *et al.*, 2007; Zaneveld *et al.*, 2001a, 2001b]. For example, the often used “ $Q$ ” factor, the ratio of upwelling irradiance to upwelling nadir radiance, has been shown to be much more variable than previously thought [Hirata *et al.*, 2009; Morel *et al.*, 2002; Zibordi and Berthon, 2001]. Much less work has been done to validate models with respect to the downwelling radiance field in the ocean [see Adams *et al.*, 2002], largely because few quantitative measurements exist, and as a result, there are large uncertainties with respect to sources of variation, in particular the particulate (volume) scattering coefficients [Chami *et al.*, 2006; Zhang *et al.*, 2011].

[5] Here we present and discuss variations in the measured full radiance distribution in three representative water types determined from a new, very high dynamic range, camera system. Unlike previous measurements, the new system can image and resolve the downwelling field in near-surface waters at sea, including the sun, at high frequency simultaneously with measurements of the upwelling field. Measurements are made from a tethered free fall platform away from the influence of perturbations by the ship.

### 2. Background and Bases

[6] Radiance is a fundamental quantity of interest in marine optics and modeling [Mobley, 1994]. It is defined as the radiant power (or photon flux) in a specified zenith and azimuth direction per unit solid angle, per unit area normal to the incident beam at a given wavelength and at a given depth and time in the ocean [Jerlov, 1976; Kirk, 1994; Mobley, 1994]. It represents the angular and spectral structure of the light field and varies with time, location, and depth due to modification of the incident surface radiance field by the sea surface, the inherent optical properties of the

<sup>1</sup>Department of Oceanography, Dalhousie University, Halifax, Nova Scotia, Canada.

<sup>2</sup>Satlantic, Inc., Halifax, Nova Scotia, Canada.

<sup>3</sup>Department of Physics, University of Miami, Coral Gables, Florida, USA.

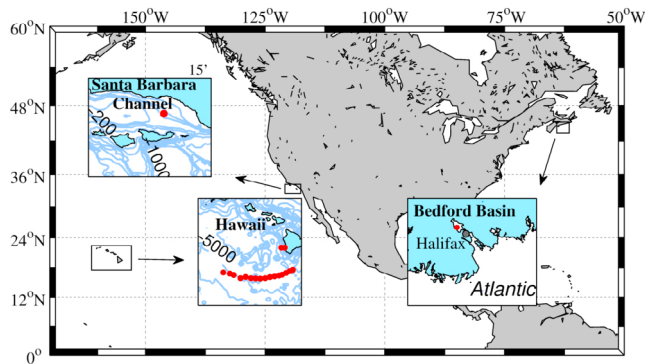


**Figure 1.** Experiment locations in the Santa Barbara Channel, California; the Pacific Ocean; off Hawaii; and the Bedford Basin, Nova Scotia. The stations have been denoted as red dots.

ocean interior, internal sources, and the reflectivity of the sea bottom [Aas and Højerslev, 1999; Mobley, 1989; Morel and Gentili, 1993; Morel et al., 1995; Preisendorfer, 1959; Tyler, 1960; Voss et al., 2003]. Along a particular path, the variation in the radiance is given by the canonical radiative transfer equation

$$\frac{dL}{dr} = -cL + L_*^E + S, \quad (1)$$

where the change in radiance along a given path,  $r$ , is given by the diminution as a result of absorption and scattering out of the beam, as represented by the beam attenuation coefficient  $c$  and the augmentation resulting from scatter into the direction of propagation from photons traveling along other paths,  $L_*^E$ . The latter is represented by the angular integration of the radiance field convoluted with the volume scattering function,  $\beta$ . For much of the spectrum, sources,  $S$ , such as Raman scattering or fluorescence, contribute as well [see Morel, 1974]. The spectral dependency is implicit and will be suppressed in what follows. Usually, horizontal variations are assumed small by comparison to those in the vertical, but even in a restricted spatial domain, high wave number variance exists as well in the horizontal ( $x, y$ ) as a result of refraction/reflection from the ruffled sea surface [Zaneveld et al., 2001a].

[7] As a fundamental quantity, the radiance distribution and its gradients can be used to derive all other radiometric quantities and all optical properties. In particular, the various irradiances are derived by weighted integration of the radiance field over defined solid angles. The downwelling ( $E_d(\lambda)$ , units of  $\mu\text{Wcm}^{-2}\text{nm}^{-1}$ ) and upwelling ( $E_u(\lambda)$ , same units) plane irradiances are given as the cosine-weighted integration of the radiance distribution over the upper (downwelling) and lower (upwelling) hemispheres, respectively, separated by a horizontal surface oriented normal to the local gravity vector. Their sum is useful to define the flux of energy across a given depth horizon in the ocean. Scalar irradiances can be derived as well from the unweighted integration over various angular domains. The scalar irradiance is indispensable for primary production estimates [Morel, 1991]. The distribution functions (e.g., the average cosines) are computed directly, as are the various

diffuse attenuation coefficients and reflectances [Mobley, 1994].

[8] In principle, measurement of the full radiance distribution, and its depth derivatives, permit not only the computation of apparent optical properties (AOPs) which depend on the angular structure of the radiance field [Preisendorfer, 1976], but also all of the important inherent optical properties (IOPs), which do not depend upon the radiance field. For example, the well-known Gershun's [1939] relationship can be directly computed from the vertical distribution of the radiance field and the subsequent integration of the canonical radiative transfer equation. The result is a direct evaluation of the absorption coefficient [Voss, 1989b]. Another interesting opportunity is the derivation of the volume scattering coefficient [see Zaneveld and Pak, 1972] from the vertical derivative of the full radiance distribution.

[9] The underwater radiance distribution is therefore the fundamental radiometric quantity from which all other optical quantities are derived. Because of this fundamental importance, measurement of the radiance distribution received a great deal of interest in the mid-1900s [e.g., Jerlov and Fukuda, 1960; Lundgren and Højerslev, 1971; Sasaki et al., 1958; Tyler, 1960]. It is perhaps surprising however, that there have been few subsequent direct observations until recently [Voss et al., 2003]. From Højerslev [1994], a history of these measurements from the first part of the 1900s demonstrates the evolution from narrow field of view radiance sensors [Jerlov, 1976] to film cameras and mechanically scanning radiometers [Smith et al., 1970; Tyler, 1960] to the use of fisheye lens with modern imaging chips [Voss, 1989a; Voss and Chapin, 1992]. It is worth noting that despite the early interest in this quantity, the hemispheric in-water radiance distribution has only been measured quantitatively and in a radiometrically accurate way (e.g., by reference to national standards of radiance, such as NIST) in the observations of Voss and colleagues [Voss, 1989a; Voss and Chapin, 1992; Voss and Morel, 2005]. The quantitative measurement of the full radiance distribution has only been realized in a very restricted set of environmental conditions.

### 3. Methods

#### 3.1. Experiment Sites

[10] Measurements of the underwater radiance distribution were carried out in three optically diverse environments. The first data set was collected in the Santa Barbara Channel, California (Figure 1) (T. Dickey et al., manuscript in preparation, 2011). This area is a coastal region with moderate phytoplankton biomass and productivity [Anderson et al., 2008], and is an optically complex mesotrophic environment [Chang et al., 2006]. We deployed the instruments here from the R/V *Kilo Moana* at a series of stations with depths of  $\sim 150$  m in September 2008. The second field expedition was completed onboard a 15 m fishing vessel in Bedford Basin (44.70°N, 63.63°W), Nova Scotia, on 31 July 2009. This semienclosed fjord-like inlet receives nutrient inputs from the surrounding urban community, and is a typical eutrophic environment [Strain and Yeats, 1999]. Our third deployment resulted in data collected during a monthlong experiment in the open Pacific Ocean, southwest of Hawaii, from late

August to mid-September 2009, again aboard the R/V *Kilo Moana*. The cruise track followed the drift of the accompanying R/V *FLIP* over approximately 300 km through these clear oligotrophic waters (see T. Dickey et al., manuscript in preparation, 2011)

[11] According to Jerlov's [1976] optical classification scheme, the open Pacific Ocean represents oceanic water type I with maximum above-water spectral reflectance in the deep violet (near 400 nm), the Santa Barbara Channel site corresponds to Jerlov's oceanic water type III, with spectral reflectance highest in the green (512 nm) and the Bedford Basin site represents Jerlov's coastal water type 5 with maximum reflectance at ~550 nm.

### 3.2. Imaging the Underwater Radiance Field

#### 3.2.1. Camera

[12] A high dynamic range radiance distribution camera system (RadCam, Satlantic, Inc.) was used to image the radiance field. The camera uses a fisheye lens and maps an entire hemisphere of the radiance field onto a complimentary metal-oxide semiconductor (CMOS) array. The resulting gray scale images were converted to radiance distributions with high intrascene dynamic range (up to  $10^6$ ), based on absolute radiometric calibrations [Mueller and Austin, 1995; Van Dommelen et al., 2010]. In general, several methods are available to achieve a high dynamic range, resulting in a logarithmic or piecewise-linear response curve. The RadCam array is partly piecewise linear, but the complete curves are more complex. Many on-chip registers are used to define the exposure time and shape of the response curve. Through experimentation, we selected three sets of register values. These exposures cover low, mid-, and high partly overlapping radiance ranges. The mid and high exposures each cover a radiance range of nearly six decades and the total range across all register values is about 9–10 decades. Exposure times range from 0.02 to 1.0 s. The optical system includes a dome (for the underwater cameras), a fisheye lens with a field of view of  $180^\circ$ , a bandpass filter centered at 555 nm ( $\pm 0.2$  nm) and with a 20 nm (full-width half-maximum) bandwidth, and an out of band rejection of  $10^{-6}$ . Relay lenses are used to focus and shrink the image from the fisheye lens so that it fits on the imaging array. The resulting image has a diameter of about 400 pixels. The resolution is about  $0.5^\circ$  at nadir and for most of the field, dropping to about  $1^\circ$  at large field angles. Roll-off (decrease in light throughput at larger field angles) is minimal.

#### 3.2.2. Calibration and Characterization

[13] Calibration of the cameras includes several steps, similar to those used by Voss and Zibordi [1989]. The first step, performed on the array without optics, is to measure the digital response of the array to a light source of variable intensity. This results in a response curve for each pixel. The second step involves measuring the response of the assembled camera to a known radiance, thus fixing the relative response curves to an absolute radiance. In this procedure, all optical elements are included. For low and middle ranges, a stable incandescent lamp serves this purpose. The lamp is not sufficiently intense for the high end of the response curves however, and a second method is then used which involves scanning across the array with a HeNe laser. The laser beam provides a very high intensity, small diameter, Gaussian beam. A single pixel is used to measure

the beam profile and determine the radius (in pixels) that is suitably uniform to be used for calibration. The array is then scanned by the laser, building up a composite calibration image. The complete response curve is then divided into sections that can be approximated by analytic functions. The array is then assembled with the optics, including the dome and a so-called system calibration is performed to fix each response curve to a known radiance using an integrating sphere with one or two arc lamps as inputs. During the calibration, the camera is rotated in front of the exit port of the integrating sphere so that each pixel points toward a uniform radiance. The radiance from the sphere is verified with a hyperspectral radiance sensor (HyperOCR, Satlantic, Inc.) operating as a secondary standard; this indirect measurement is required to achieve accuracy at the high radiances required. Combined uncertainties in the transfer to the HyperOCR have been determined to be 2.5% in the vicinity of 555 nm [Voss et al., 2010]. Geometric calibrations are then performed to find the image center and radius.

[14] We determined the immersion factor and point spread function of the cameras. The immersion factor is a single value that scales the measured radiance values to account for the change in pixel field of view above and below water. It cannot be determined theoretically as with a simple Gershun tube radiometer [see Mueller and Austin, 1995] and requires a vicarious characterization using secondary standards of radiance.

[15] The point spread function (PSF) describes the scattering of light from the intended pixel to other surrounding pixels. When imaging the sun, which may have radiance several orders of magnitude higher than nearby pixels, it has a significant impact. We measured the PSF by expanding a green HeNe beam and directing it at the completed camera. To the camera, the beam is a distant point source and would ideally image to a single pixel. The actual spread in the image represents the PSF. Further work on the PSF involved using the radiance camera mounted under clear skies, and with comparisons made between total sky images, and those with the sun occluded.

[16] The resulting radiometrically calibrated images have radiance values (unit:  $\mu\text{Wcm}^{-2}\text{sr}^{-1}\text{nm}^{-1}$ ) for each pixel in the array, corresponding to a defined zenith angle,  $\theta$ , and relative azimuth angle,  $\varphi$ , with respect to the camera reference frame.

[17] All radiance distributions were subject to further geometrical transformation to account for the tilt and heading errors. For the upwelling radiance field, we extrapolated the radiance near the horizon where some pixels were lost during the tilt corrections.

#### 3.2.3. Deployment of the Camera Systems

[18] The underwater unit of the RadCam was built as a 1 m long cylindrical tethered free fall [see Waters et al., 1990] package, with a 10 cm diameter. Cameras were installed at each end, one looking upward and the other facing down. In this way, the downwelling radiance field and upwelling radiance field were measured simultaneously. Ancillary sensors were integrated with this package. They included simultaneous measurements of the tilt, roll, and heading of the instrument, and conductivity, temperature and pressure. A four spectral channel upward looking irradiance sensor and a downward looking four-channel radi-

ance sensor (Satlantic OCR 504I/R) were attached to the vehicle to provide validation data. A WET Labs' transmissometer was also used to measure the beam attenuation coefficient (532 nm) of the water when the radiance field was imaged.

[19] A reference camera was set up on the ship's upper deck to monitor the sky radiance distribution including the sun. A reference irradiance sensor (HyperOCl; Satlantic) was also set up to measure above-water downwelling spectral irradiance  $E_s(\lambda)$ . All sensor observations, consisting of the radiance cameras, radiometers, transmissometer, CTD and tilt sensor, were synchronized with a GPS time signal to within 5 msec absolute accuracy.

[20] In the Pacific Ocean and the Santa Barbara Channel, the tethered underwater RadCam package was deployed from R/V *Kilo Moana*. The free fall vehicle system was deployed from the stern of the vessel, which had headway of  $\sim 0.5 \text{ m s}^{-1}$ . At least a 50 m distance from the stern was generally retained before the vehicle was released and started profiling the water column with a drop rate of  $\sim 0.5 \text{ m s}^{-1}$ . With a camera sampling rate of 4 Hz, it took approximately 1.5 min to complete the scanning of the water column to 50 m depth with a depth resolution of  $\sim 10 \text{ cm}$ . In Bedford Basin, the camera was released from a position about 10 m away from a small boat. A sampling rate of 1 Hz was used and profiles were taken to 20 m.

### 3.3. Data Analyses

[21] We calculated the solar zenith angle,  $\theta_s$ , from the geophysical coordinates and the time of observation [Reda and Andreas, 2004]. In Pacific Ocean,  $\theta_s$  was generally limited to  $< 30^\circ$  while the water column was profiled. For the Santa Barbara Channel experiment,  $\theta_s$  was between  $40^\circ$  and  $50^\circ$ . In Bedford Basin, our casts were retrieved when the solar zenith was at  $\theta_s = 43^\circ$ . Relative azimuth was computed from astronomical calculations based on location and time, and the measured compass heading of the instrument onboard the vehicle.

[22] The sky conditions were classified based on the all-sky radiance observations. Ideal, completely clear skies were rarely met at sea. Rather there often existed some clouds in the midzenith angles to the horizon. For the following computations, we treated these situations as clear skies as long as the sun was not directly blocked. Since the radiance distribution profile was usually retrieved in a very short time, no quantitative efforts were made to identify variations in the sky conditions.

[23] Irradiances from the radiance cameras were derived from the measured radiance distribution based on integration schemes [Wei et al., 2010]. For example, the downwelling plane irradiance,  $E_d$ , can be calculated as

$$E_d(z) = \sum_{i=1}^{i=I} \sum_{k=1}^{k=J} L(i, j, z) \cos \theta_{ij} \Omega_{ij}, \quad (2)$$

where  $\Omega_{ij}$  is the solid angle subtended by pixel indexed by  $(i, j)$ , which corresponds to a location with central zenith angle  $\theta_{ij}$ , and  $L(i, j, z)$  is the radiance recorded by pixel  $(i, j)$  at depth  $z$ . The solid angles  $\Omega_{ij}$  and zenith angles  $\theta_{ij}$  represented by each pixel were determined by the projection geometry of the camera. We calculated the solid

angles with the following equation [also see Voss and Chapin, 2005]:

$$\Omega_{ij} = \frac{\pi}{D l_{ij}} \cdot \sin\left(\frac{\pi l_{ij}}{D}\right), \quad (3)$$

where  $D$  is the image diameter and  $l_{ij}$  is the radial distance for pixel  $(i, j)$ , restricted to the imaged hemisphere. For a  $180^\circ$  field of view camera, the zenith angle at pixel  $(i, j)$  was expressed as

$$\theta_{ij} = \frac{2l_{ij}}{D} \cdot \frac{\pi}{2}. \quad (4)$$

The diffuse attenuation coefficients for directional radiance profiles and irradiance profiles were determined with the integration method [Zaneveld et al., 2001a]. This method is suitable for depth profiles which generally follow an exponential law, and was used for profiles of 0–40 m in Pacific Ocean, 0–20 m in the Santa Barbara Channel, and 0–5 m in the Bedford Basin.

[24] The average cosine for the full radiance distribution is calculated as

$$\bar{\mu}(z) = \frac{E_d(z) - E_u(z)}{E_o(z)}, \quad (5)$$

where  $\bar{\mu}$  is the average cosine,  $E_u$  is the upwelling plane irradiance, and  $E_o$  is the scalar irradiance. The  $Q$  factor is expressed as the ratio of  $E_u/L_u$ , where  $L_u$  is the nadir radiance (or  $L(\theta = 180^\circ)$ ).

[25] The total absorption coefficient,  $a$ , can be computed following Gershun's [1939] law

$$\nabla \cdot \mathbf{E} = aE_o, \quad (6)$$

where the divergence in the vector irradiance ( $\mathbf{E}$ ) as well as the scalar irradiance can be computed directly, or equally (assuming horizontal components of the divergence small by comparison to the vertical, and in the absence of internal sources) from

$$a(z) = \bar{\mu}(z)K_{\text{net}}(z), \quad (7)$$

where the  $K_{\text{net}}$  is diffuse attenuation coefficient for the net downward irradiance.

### 3.4. Simulations of the Radiance Distribution

[26] With the measured sky radiance distribution, we simulated the underwater radiance field using code developed by one of us (J. Wei, unpublished material, 2011). A backward Monte Carlo scheme was used, which traced the photon from the sensor to the source [Collins et al., 1972]. The idealized radiance sensor had a  $1^\circ$  (half angle) field of view. The water body was assumed homogeneous and infinitely deep. The optical absorption coefficient and scattering coefficient were taken as averages from direct measurements by a WET Lab's ac-9 m (M. S. Twardowski et al., manuscript in preparation, 2011) deployed about 1 h earlier than the RadCam casts in the Pacific Ocean. The averaged Petzold's scattering phase function [Mobley et al., 1993] was adopted in the Monte Carlo model. The air-sea interface was simulated by a Gaussian model [Cox and Munk, 1954], which

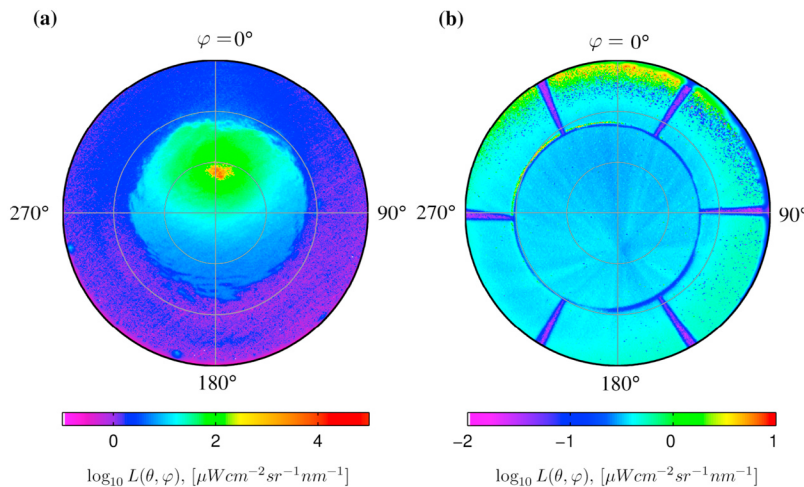


**Figure 2.** Polar plots of the (a) downwelling radiance distribution and (b) upwelling radiance distribution under clear skies. The animation is available in the auxiliary material. The data are collected at 2 m depth beside the Big Island of Hawaii ( $155^{\circ}58' \text{ W}$ ,  $19^{\circ}15' \text{ N}$ , 27 August 2009, 20:40 UTC), with wind speed of  $1.5 \text{ m s}^{-1}$  and solar zenith angle  $30^{\circ}$ .

depends on the wind speed above the sea surface. For each model run, there were a total of  $10^7$  photons being traced. To facilitate the model-data comparison, we used the radiance distribution measurements collected under one of the most favorable sea state conditions, when the wind speed was only  $1.5 \text{ m s}^{-1}$  and sea surface was fairly smooth.

## 4. Results

### 4.1. Hemispheric Radiance Fields

[27] Figure 2 illustrate typical radiance distributions at near-surface depths in the clear waters off Hawaii. Each panel presents the hemispheric radiance field defined in polar coordinates. The coordinate's origin corresponds to either the zenith direction ( $\theta = 0^{\circ}$ ) for the upper hemisphere ( $0^{\circ} \leq \theta \leq 90^{\circ}$ ) or the nadir direction for the lower hemisphere ( $90^{\circ} \leq \theta \leq 180^{\circ}$ ). The zenith angle along the image edge in both hemispheres is equal to  $\theta = 90^{\circ}$ , i.e., the horizon. The zenith angle changes linearly from the origin to the horizon. The relative azimuth angle is labeled along the horizon; the direction of the sun (i.e.,  $\varphi = 0^{\circ}$ ) is at the top of the figure. Each pixel gives the directional radiance in a specific direction ( $\theta, \varphi$ ). The radiance field in each hemisphere has an angular resolution  $\Delta\theta$  of  $0.45^{\circ}$  along the radial direction. Along the azimuthal direction, however, the angular resolution depends on the radial position. For example, the  $\Delta\varphi$  increases from  $0.35^{\circ}$  when  $\theta = 10^{\circ}$  to  $2.5^{\circ}$  when  $\theta = 80^{\circ}$ . The sea surface area resolved as in the radiance map depends on water depth as well as the radial position. For the sample shown in Figure 2, the sea surface resolution  $\Delta A$  near the zenith direction is about  $2 \text{ cm}^2$ . Away from the zenith direction, the surface resolution becomes coarser.

[28] Figure 2a gives an example for the downwelling radiance distribution under sunny skies. In the near-surface radiance field a clear Snell's window is evident, which is defined as a conic region with  $\theta = 48.6^{\circ}$ . The Snell's extinction boundary generally divides the hemisphere into light refraction region ( $\theta < 48.6^{\circ}$ ) and internal reflection

zones ( $\theta > 48.6^{\circ}$ ); the all-sky radiance is therefore concentrated within the Snell's window. It is noted that, however, the boundary is often disrupted by surface waves even for the calmest of sea states. For these conditions, the Snell's window is roughly symmetric about the zenith.

[29] Another prominent feature with the downwelling radiance field is the refracted glitter pattern of the sun, i.e., the glitter as seen from beneath the surface [Cox and Munk, 1956]. Depending on the surface roughness, the refracted sun splits into several or many irregularly distributed image fragments. For example, many pixels in Figure 2a have measured radiances higher than  $1000 \mu\text{Wcm}^{-2}\text{sr}^{-1}\text{nm}^{-1}$ ; these numbers exceed those in the all-sky radiance distribution measured above the surface. The refracted sun images in a given scene constitute an instantaneous glitter pattern which varies considerably with the passage of individual waves, with the location of the glitter often translated away from the  $0^{\circ}$  in azimuth as a result of surface waves. Such a dynamic radiance distribution observed by the RadCam is available in auxiliary material (with Animation S1, which shows the temporal variation of the light field).<sup>1</sup>

[30] Figure 2b shows an interesting example for the upwelling radiance field. The data are close to the same depth horizon as in Figure 2a in the Pacific Ocean. The upwelled radiance field takes a more uniform appearance than its downwelling counterpart. The intrascene dynamic range spans only 2 orders of magnitude in surface waters by comparison with six in the corresponding downwelling scene. Some alternating bright and dimmer light beams are evident which converge to a point corresponding to the instrument's shadow in the antisolar direction. The self-shaded shadow is not evident for these clear waters, but is common to all downward looking sensors [also see Smith, 1974; Voss and Chapin, 2005]. According to Gordon and Ding's [1992] method, our measurement could underestimate the nadir radiance  $L(\theta = 180^{\circ})$  by  $<5\%$  as a result. The

<sup>1</sup>Auxiliary materials are available in the HTML. doi:10.1029/2011JC007275.

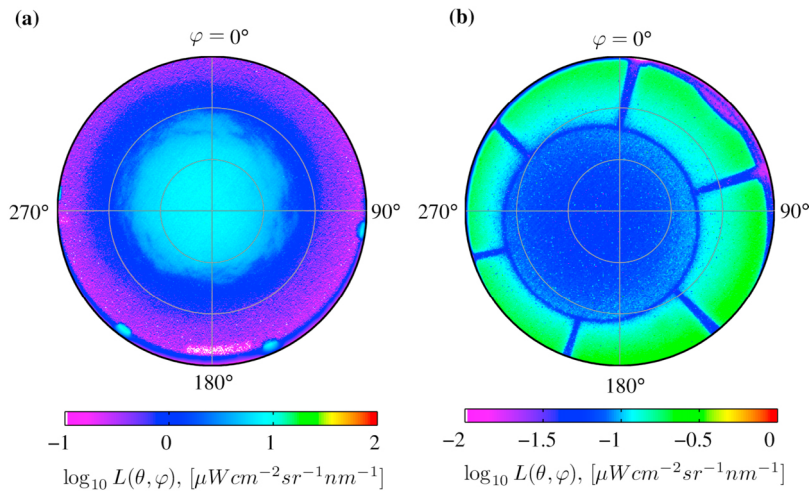


**Figure 3.** Polar plots of the (a) downwelling radiance distribution and the (b) upwelling radiance distribution under overcast skies. The data are from a depth of 1.75 m in the Santa Barbara Channel, California (13 September 2008, 17:40 UTC), with wind speed  $5 \text{ m s}^{-1}$ .

bright and dark light beams are most evident at lower wind speeds ( $1.5 \text{ m s}^{-1}$  in this case). The brightening on the horizon near the direction of the sun is a consequence of scattering from the solar beam and adjacent sky.

[31] Figures 3a and 3b show the downwelling and upwelling radiance fields under overcast skies in the Santa Barbara Channel but at a higher wind speed ( $5 \text{ m s}^{-1}$ ). In this case, the scene dynamic range is much lower so a different color scale is used for better presentation. The wavy patterns observed are a result of the ruffled sea surface [e.g., Hubbard *et al.*, 2006]. No clear-cut Snell's window is observed. The instrumental shading effect cannot be easily identified.

[32] Some artifacts are present in our measurements. The telemetry cable is often seen in the upper hemisphere,

screws are recorded at the horizon, and the guard framework is evident in the upwelling image. The effects are minor for the downwelling image considering the highly anisotropic light distribution. The blocking of light by the guard framework for the upwelling field will cause an underestimate for the scalar irradiance, but no more than 5%, an error that can be reduced to less than 1% by simple interpolation across the affected pixels.

#### 4.2. Depth Evolution of Radiance Distribution

[33] Figure 4 depicts the depth progression of radiance in selected directions in the three environments sampled. The respective solar zenith angles are given in Table 1. The radiance profiles in Figure 4a have spatial resolutions in the vertical of  $\sim 10 \text{ cm}$ , corresponding to temporal resolution

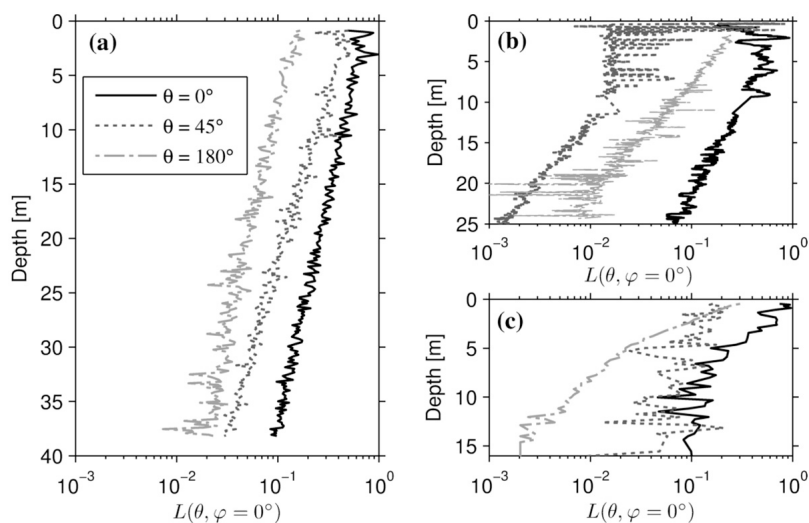


**Figure 4.** Depth profiles of relative radiance for different zenith angles in the plane of the sun under sunny skies. (a) Pacific Ocean, depth resolution is 10 cm. (b) Santa Barbara Channel, California, depth resolution is 5 cm. (c) Bedford Basin, Nova Scotia, depth resolution is 20 cm. The directional radiance has been arranged along the abscissa axis to attain a clear comparison.

**Table 1.** Comparison of the Diffuse Attenuation Coefficients ( $\text{m}^{-1}$ ) for the Directional Radiance  $K_{L(\theta, \varphi)}$  in the Principal Plane<sup>a</sup>

	Pacific Ocean		Santa Barbara Channel			Bedford Basin Clear Sky	
	Clear Sky, 0-40 m	Cloudy Sky, 0-40-m	Clear Sky		Cloudy Sky, 0-25 m	0-5 m	5-15 m
			0-5 m	10-25 m			
$0^\circ$	0.040	0.059	-0.053	0.101	0.121	0.433	0.108
$45^\circ$	0.059	0.0909	—	0.135	0.124	0.480	0.205
$180^\circ$	0.055	0.057	0.306	0.305	0.127	0.627	0.097
$\theta_s$	$30^\circ$	$26^\circ$	$45^\circ$	$45^\circ$	$44.5^\circ$	$43^\circ$	$43^\circ$

<sup>a</sup>Here  $\varphi = 0^\circ$ .

of 0.25 s. The profiles in Figures 4b and 4c have different resolutions. They represent profiles at different zenith angles, but in the principal plane, that is  $\varphi = 0^\circ$  (the vertical plane containing the sun in air). Note that the values plotted are relative radiances, and furthermore, the individual profiles within each figure have been offset along the abscissa for clarity in presentation.

[34] Fluctuations are found with all radiance profiles. The magnitude of the fluctuations generally decreases with water depth (increased variance at depth for  $\theta = 180^\circ$  is due to instrumental noise, not environmental variance). A near-surface maximum of radiance is sometimes observed for the downwelling radiance (e.g.,  $L(\theta = 0^\circ)$  and  $L(\theta = 45^\circ)$ ) in Figures 4a and 4b. According to the wave focusing theory [Stramski and Dera, 1988; Zaneveld *et al.*, 2001a], this location corresponds to the focal points of waves. The upwelling radiances are less affected by the waves. As pointed out by Jerlov and Fukuda [1960], the observed maxima can be generated as well in the absence of surface waves by refraction and scattering in the ocean interior. For directions close to the refracted glitter pattern, the radiance values might vary by several orders of magnitude within a very short period of time (Figure 4b,  $\theta = 45^\circ$ ).

[35] Except for the fluctuations, it follows from Figure 4 that below the depth of the local maximum, the decrease of radiance in the Pacific Ocean waters can be represented by the exponential law  $\exp(-zK_L)$ . In complex waters of the Bedford Basin, a noticeable biphasic variation is found; it is associated with an intense subsurface layer of phytoplankton. A comparison of the diffuse attenuation coefficient for the directional radiance,  $K_L$ , is summarized in Table 1.  $K_L$  is directionally specific, dependent on the sky conditions, and is also a function of water inherent optical properties. In most cases, the zenith radiance diminishes more slowly than the upwelling nadir radiance; a systematic relationship remains to be explored.

[36] The depth evolution for the angular radiance distribution in the principal plane is given in Figure 5. All the plots are chosen from the hemispheric radiance distributions which have a glitter pattern or a maximum radiance aligning with the ideally refracted sun's direction ( $\varphi = 0^\circ$ ). The most evident feature of the data is the high transparency of the Pacific Ocean water with the highest intrascene dynamic range radiance. The maximum radiance has only been slightly shifted toward the zenith from 5 m to 45 m. Other conspicuous features can be identified after a close

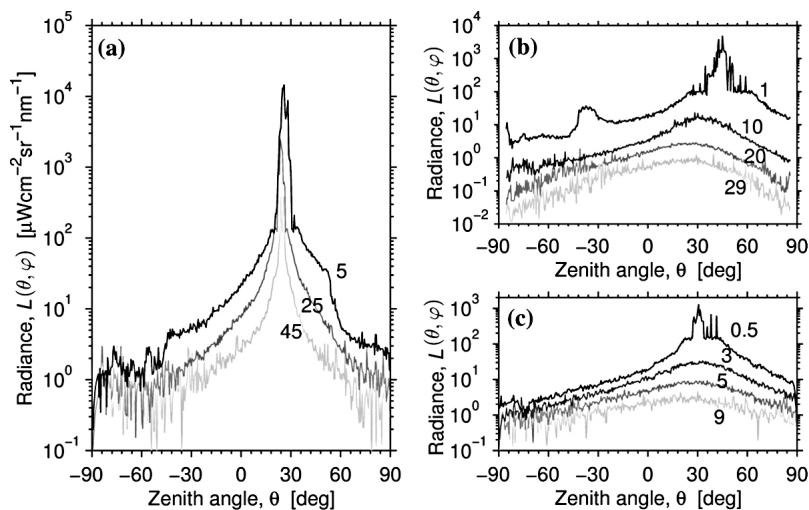


**Figure 5.** Radiance distribution in the principal plane as measured in three waters. All radiance values presented are in absolute units; each curve represents a different depth denoted by the adjacent value (m). The positive angles refer to the directions at the same azimuth with the sun. The antisolar directions are denoted by negative angles. (a) Data in the Pacific Ocean, off the Big Island of Hawaii, on 27 August 2009, 20:40 UTC, sunny and a little hazy sky, wind speed  $1.5 \text{ m s}^{-1}$ . (b) Data in the Santa Barbara Channel, California, on 10 September 2008, 23:00 UTC, clear sky, wind speed  $7 \text{ m s}^{-1}$ . (c) Data in the Bedford Basin, Nova Scotia, on 31 July 2009, 19:00 UTC, clear sky, wind speed  $6 \text{ m s}^{-1}$ .

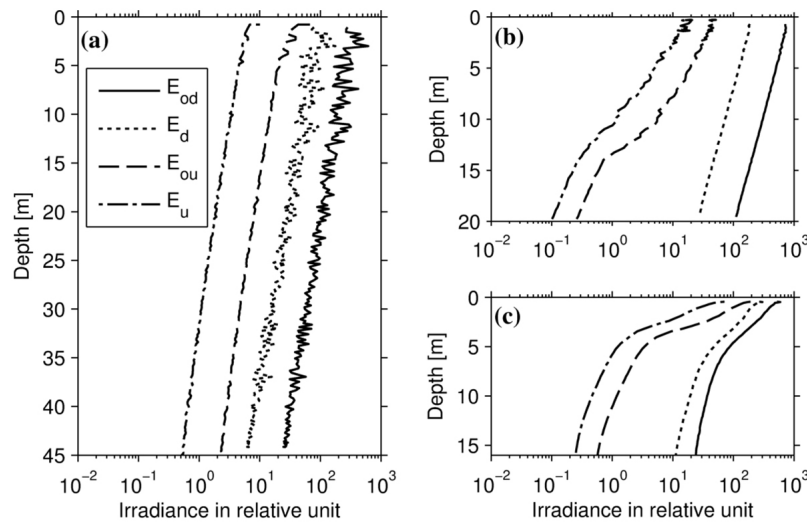


**Figure 6.** Irradiance varying with water depth as derived from the radiance distribution measurements. Only the relative values are given for a clear comparison. (a) Data in the Pacific Ocean, off the Big Island, Hawaii, collected on 27 August 2009, 20:40 UTC. (b) Data in the Santa Barbara Channel, California, obtained on 13 September 2008, 17:30 UTC. (c) Data in the Bedford Basin, Nova Scotia, measured on 31 July 2009, 19:00 UTC.

inspection. The peaks for the maximum radiance are usually broad, with high radiance value spikes scattered around the maxima associated with the glitter pattern. In coastal waters, the radiance diminishes much faster with depth. The research vessel we used is occasionally captured in the fine radiance structure below the sea surface. An example is given in Figure 5b where either the reflective ship's hull or reflective clouds near the horizon generates a refracted bump at  $\theta = 40^\circ$  in the 1m radiance distribution curve.

#### 4.3. Irradiance Distribution

[37] An application of the radiance distribution is the derivation of the scalar irradiances ( $E_{od}$  and  $E_{ou}$ ) and the vector irradiances ( $E_d$  and  $E_u$ ). Four families of irradiance depth profiles are plotted in Figure 6. These data show that the  $E_{od}$  depth variations are similar to the  $E_d$  profiles, and

the  $E_{ou}$  profiles behave similarly to the  $E_u$  profiles. But the downwelling light may vary with depth quite differently than the upwelling light, depending on the water homogeneity. The rate of decline of the downwelling irradiance is primarily determined by the diffuse attenuation coefficient, while the single-scattering albedo ( $b/c$ ) plays a stronger role for vertical changes in upwelling irradiance.

[38] The diffuse attenuation coefficients are strongly affected by the nonuniform distribution of chlorophyll in these waters, where the subsurface chlorophyll maximum layers were observed at 120 m, 15–25 m, and 5–7 m in the Pacific, Santa Barbara Channel, and Bedford Basin, respectively (Table 2). We found that a relation of  $K_u \leq K_d \leq K_{net}$  holds for clear Pacific Oceanic water, and of  $K_{net} < K_d < K_u$  for complex coastal waters. Hirata [2003] suggested similar relationships between diffuse attenuation coefficients

**Table 2.** Optical Properties in Three Surface Waters as Derived From the Radiance Distribution Measurement<sup>a</sup>

Optical Property	Pacific Ocean, 0–40 m		Santa Barbara Channel, 0–10 m		Bedford Basin, 0–5 m, Clear Sky
	Clear Sky	Cloudy Sky	Clear Sky	Overcast Sky	
$K_d$ ( $m^{-1}$ )	0.064	0.070	0.133	0.112	0.209
$K_{od}$ ( $m^{-1}$ )	0.062	0.069	0.133	0.106	0.272
$K_u$ ( $m^{-1}$ )	0.058	0.057	0.167	0.086	0.828
$K_{ou}$ ( $m^{-1}$ )	0.061	0.063	0.144	0.074	0.716
$K_{net}$ ( $m^{-1}$ )	0.064	0.070	–	0.113	0.153
$K_o$ ( $m^{-1}$ )	0.061	0.069	–	0.104	0.338
$\bar{\mu}_d$	$0.812 \pm 0.030$	$0.831 \pm 0.010$	$0.655 \pm 0.006$	$0.731 \pm 0.017$	$0.523 \pm 0.024$
$\bar{\mu}_u$	$0.460 \pm 0.005$	$0.452 \pm 0.031$	$0.376 \pm 0.048$	$0.418 \pm 0.025$	$0.286 \pm 0.053$
$\bar{\mu}$	$0.782 \pm 0.033$	$0.807 \pm 0.012$	–	$0.667 \pm 0.023$	$0.412 \pm 0.083$
$R$	$0.013 \pm 0.003$	–	$0.111 \pm 0.017$	–	$0.162 \pm 0.104$
$Q(0)$ (sr)	$3.379 \pm 0.187$	$3.607 \pm 0.235$	$4.087 \pm 0.199$	$4.660 \pm 0.256$	$4.478 \pm 0.533$
$\theta_s$	$31^\circ$	$26^\circ$	$53^\circ$	$44^\circ$	$43^\circ$
First optical depth (m)	16.5	14.3	7.5	9	4.8
$\overline{Chl}$ ( $mg\ m^{-3}$ )	0.04	0.04	0.86	0.78	7.17
Time and date (UTC)	20:25, 27 Aug 2009	20:50, 4 Sep 2009	23:00, 14 Sep 2008	17:30, 13 Sep 2008	19:00, 31 Jul 2009

<sup>a</sup>Radiance distribution measurement is 555 nm. The average chlorophyll concentration within the first optical depth is estimated from CTD casts made board R/V *Kilo Moana* in the Pacific and the Santa Barbara Channel; the chlorophyll concentration in the Bedford Basin is based on online data (<http://www2.mar.dfo-mpo.gc.ca/science/ocean/BedfordBasin>).

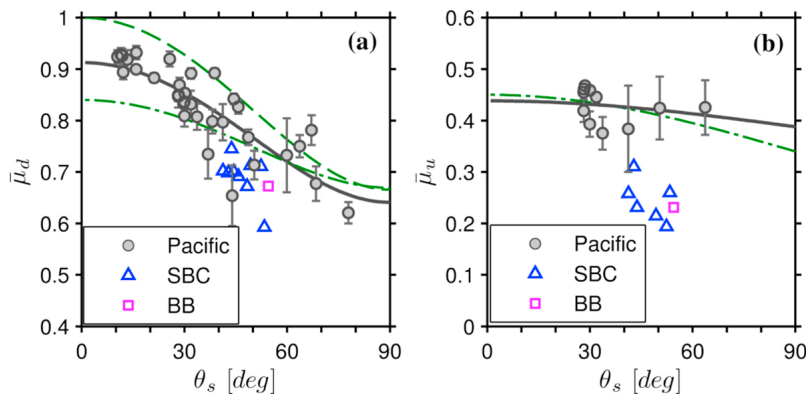


**Figure 7.** (a) The downwelling average cosine and (b) the upwelling average cosine for green light (555 nm) measured at a depth of 5 m as a function of the solar zenith angle  $\theta_s$  in three waters. The best fit solid line for  $\bar{\mu}_d$  in the Pacific Ocean is  $\bar{\mu}_d = (0.81 \pm 0.09) \cos(\theta_{sw}) + (0.1 \pm 0.08)$ , with the correlation coefficient  $r = 0.84$ ; the  $\theta_{sw}$  in the above regression refers to the refracted solar zenith angle within water, which is related to  $\theta_s$  by the Snell's law. The best fit for  $\bar{\mu}_u$  in the Pacific Ocean is  $\bar{\mu}_u = (0.05 \pm 0.07) \cos(\theta_s) + (0.1 \pm 0.08)$ . The dashed line in Figure 7a shows a model,  $\bar{\mu}_u = \cos(\theta_{sw})$ , appropriate only for collimated beam at normal incidence. The dot-dashed lines in Figures 7a and 7b are the fitted models obtained by Aas and Højerslev [1999] in the Mediterranean Sea.

from a theoretical perspective. His conclusion is now affirmed in light of our field observations. The relative enhancement of the upwelling field and the depression of  $K_u$  as a result of Raman scattering in clear ocean waters contributes to the observed inequality as well.

#### 4.4. Distribution Functions

[39] Figure 7 describes the measured average cosines at 5 m depth as a function of the solar zenith angles in surface seawaters. The downwelling average cosine,  $\bar{\mu}_d$ , in clear oceanic waters can be satisfactorily approximated by a linear function of the cosine of the solar zenith angle  $\theta_s$ . The upwelling average cosine is only weakly dependent on the solar angle. The average cosines at the same depth, from the Santa Barbara Channel and the Bedford Basin, have lower values than the clear oceanic waters. Due to the limited number of observations, no statistics have been computed for these two environments.

[40] The nadir value for the ratio of upward irradiance to upward radiance ( $Q$ ; sr) increases across the progression from clear oligotrophic waters to turbid coastal environments. Our measurements of the upwelling radiance field return a  $Q$  value for nadir radiance of  $3.38 \pm 0.19$  sr near the sea surface for clear-sky days in the oligotrophic Pacific, increasing to  $4.09 \pm 0.20$  sr in Santa Barbara Channel to  $4.48 \pm 0.53$  sr in the eutrophic Bedford Basin. The distribution functions are tabulated in Table 2.

#### 4.5. Inherent Optical Properties

[41] We demonstrate in this section the inversion of some inherent optical properties from the radiance distribution data. Figure 8a gives the absorption coefficients in Pacific Ocean estimated from equation (7). The derived absorption coefficients are found to be lower than in situ measured absorption coefficients by about 10–25% within the 0–40 m water column. In the Santa Barbara Channel, the downwelling and upwelling radiance distribution were measured separately in time, so did not give an accurate estimate for

$\bar{\mu}_d$ . We started the inversion with the following expression [Hirata and Højerslev, 2008],  $K_d(z)\bar{\mu}_d \approx a(z) + b_b(z)$ , where  $b_b$  represents the backscattering coefficient and this expression holds for surface waters where  $E_{od} \gg E_{ou}$  holds. Figure 8b shows the results for  $(a + b_b)$  in the Channel. The noticeable three-sectional variation of the derived absorption is principally a consequence of the  $K_d$  estimation, for which we divided the  $E_d$  profile into three segments and calculated a mean  $K_d$  separately for each section. For the Bedford Basin experiment, there was no alternate measurement of water inherent optical properties available for a direct comparison. We computed an average absorption coefficient of  $0.131 \text{ m}^{-1}$  for 1–5 m water. Historical ac-9 measurements in this region give an absorption coefficient of  $0.107 - 0.138 \text{ m}^{-1}$ , from November 2008 to early June 2009.

#### 4.6. Comparison of Radiance Data

[42] In this section we compare the radiometric measurements derived from the camera measurements of the radiance distribution with independent measurements of these radiometric parameters. The depth profile of the upwelling nadir radiance  $L_u$  and downwelling plane irradiance  $E_d$  from the OCR-504 radiometers are chosen for field data validations. The OCR-504R measured the  $L_u$  with a field of view of  $\alpha_{1/2} = 11.5^\circ$ . To be consistent, the RadCam data was weighted and averaged for neighboring pixels around the nadir direction, to result in an observation that subtends an equivalent solid angle with the OCR-504R. The resultant data sets are compared in Figure 9a. Very good agreement is achieved for these two sets of data (Pearson correlation coefficient  $\rho = 0.995$ ,  $P < 0.001$ ).

[43] We then proceed with comparing the absolute values of  $E_d$  derived from the radiance distribution to the OCR-504I measurements of downwelling irradiance in Figure 9b. Again, the two data sets show good agreement throughout the water column (Pearson correlation coefficient  $\rho = 0.869$ ,  $P < 0.001$ ). It is noted that the  $E_d$  data agreement is not as

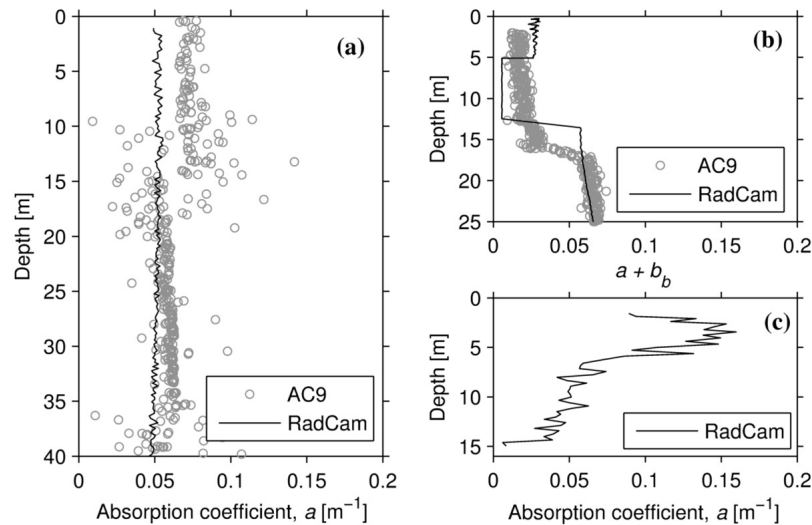


**Figure 8.** Estimation of the inherent optical properties from the radiance distribution data in (a) Pacific Ocean, on 27 August 2009, 20:37 UTC; (b) Santa Barbara Channel, California, on 15 September 2008, 17:35 UTC; and (c) Bedford Basin, Nova Scotia, on 31 July 2009, 19:00 UTC. The ac-9 data are overlaid in Figure 8a for the absorption coefficient only and in Figure 8b for the sum of absorption coefficient and the backscattering coefficient.

good as  $L_u$ 's. Apart from the instrumental calibration errors, large horizontal gradients in the downwelling light field below surface waves [e.g., Zaneveld *et al.*, 2001a] may be responsible for this. Furthermore, the effective surface area of two sensors used is also somewhat different. We analyzed the data sets under cloudy skies, and found they generally showed better agreement (for example  $\rho = 0.988$ ,  $P < 0.001$  for downwelling irradiance at another Hawaii station under cloudy skies). For the radiance distribution in the vertical plane, we compared the measurements with the Monte Carlo model simulated results. For the Pacific waters, the model used an absorption coefficient of  $0.06 \text{ m}^{-1}$ , and a scattering coefficient of  $0.03 \text{ m}^{-1}$ . The hemispheric radiance distribution chosen for comparison had a very small glitter pattern and the refracted sun is close to its theoretical position under plane sea surface. Both the simulated and measured radiance

distributions are given in Figure 10. Note that the simulations give relative radiance rescaled to the measured upwelling nadir radiance, and the two data sets have shown satisfactory agreement.

## 5. Discussion

[44] A new means to explore the fundamental radiance distribution and its sources of variability is presented. The simultaneous upward and downward hemispheric cameras, which resolve angles less than a degree, and which operate at high scene dynamic range and at high temporal resolution is a novel accomplishment. The simultaneous measurement of the sky (plus sun) radiance distribution allows the evaluation of the influence of both the sea surface roughness and in-water inherent optical properties in shaping the evolution of the radiance distribution with depth. The data set col-

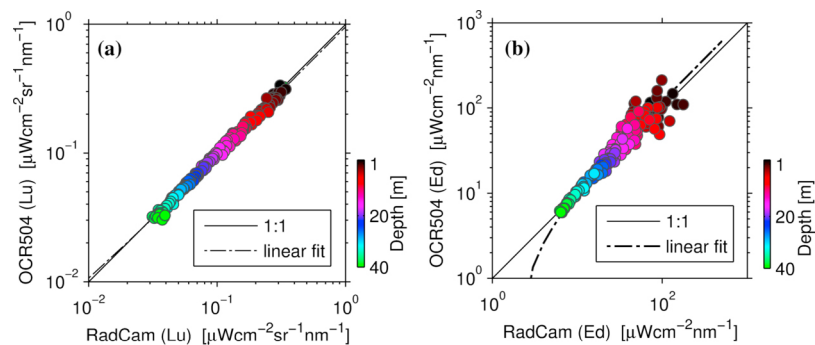


**Figure 9.** Comparison of the radiance and irradiance measurements. (a) The upwelling nadir radiance collected by RadCam and OCR-504R radiometer in the Pacific Ocean, on 27 August 2009, 20:15 UTC; the least squares linear fit is calculated as  $y = 0.945x + 0.002$ , with Pearson's correlation coefficient  $\rho = 0.995$ ,  $P < 0.001$ . (b) Downwelling plane irradiance measured by the RadCam and the OCR-504I radiometer in the Pacific Ocean, on 27 August 2009, 20:15 UTC; the least square fit is  $y = 1.129x - 1.450$ , correlation coefficient  $\rho = 0.869$ ,  $P < 0.001$ . The sky was pretty clear.

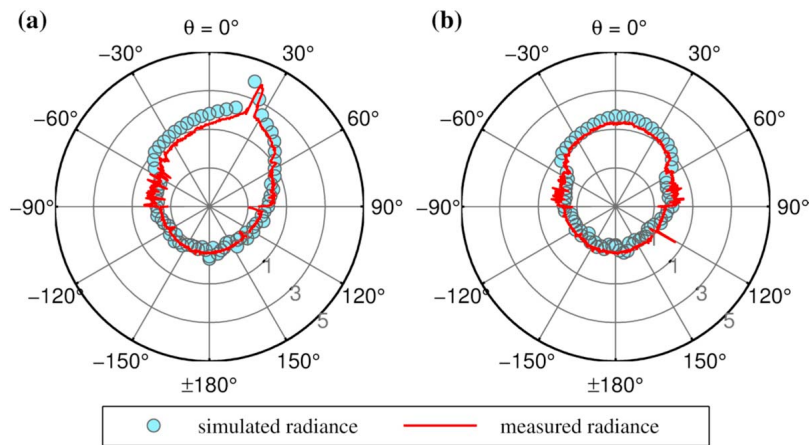


**Figure 10.** Polar plots of the relative radiance distribution (a) in the principal plane and (b) in the perpendicular plane at water depth of 5.8 m in the Pacific Ocean. The modeled radiance is normalized to the measured nadir radiance. Both are represented in logarithmic scales. Solar zenith angle is  $29^\circ$  in air. The zenith angles have been labeled. The  $0^\circ$  represents the zenith, and the  $\pm 180^\circ$  points to the nadir. In the principal plane; the positive angles refer to the azimuth direction of the sun, i.e.,  $\varphi = 0^\circ$ , with negative angles corresponding to the antisolar direction,  $\varphi = 180^\circ$ . In the perpendicular plane, positive angles and negative angles are directions along  $\varphi = 90^\circ$  and  $\varphi = 270^\circ$ , respectively. A radiometer with half angle,  $\alpha_{1/2} = 0.25^\circ$ , is simulated in the model.

lected permits the diagnosis of variations in inherent optical properties, and the validation of forward models of radiative transfer in the sea.

[45] The radiance distributions given in Figures 2 and 3 represent the first near-surface simultaneous observations of the full radiance distribution. For the downwelling fields, the clear waters of the Pacific yield very high dynamic ranges as a result of the low attenuation and the relative strength of the absorption coefficient relative to the scattering coefficient in these waters; this allows the radiance from the refracted sun to enter into a limited angular range. The resulting radiance distribution (Figure 5) is therefore strongly peaked, approaching the theoretical limit in cross section across the solar plane when absorption dominates the attenuation coefficient [Preisendorfer, 1959]. This is in contrast to the more turbid coastal and eutrophic waters that had higher scattering albedos that resulted in a flattening of the field; dynamic ranges were more than 2 orders of magnitude smaller at comparable optical depths in the Santa Barbara Channel relative to those in the Pacific.

[46] For the clear Pacific waters and for Santa Barbara Channel, almost all of the dynamic range in the downward direction and all of the information regarding the above-water radiance distribution is contained within the well-defined Snell's cone. This is particularly evident for calm sea states where the edge of the Snell's cone is sharply defined and where there is little radiance in the region between the edge of the Snell's cone and the horizon. For the highly scattering eutrophic waters, the Snell's cone is not evident.

[47] For the upwelling fields, the dynamic range is much reduced, and a much more uniform field is seen in all water types, again consistent with theory and other observations [see Voss et al., 2007].

[48] At greater depths, the downwelling field becomes more uniform; the rapidity with which this occurs varies

with the relative importance of scattering in the medium. The angle of greatest radiance migrates to zenith. For the upwelling field, the proportionate change in the relative distribution is small. The depth progression of the radiance distribution is generally consistent with previous analyses [Jerlov and Fukuda, 1960; Lundgren and Højerslev, 1971; Tyler, 1960], except that the dynamic fine structures have been revealed in the hemispheric radiance map. The radiance near the refracted sun is subject to great variability related to dynamics of the sea surface wave slopes [Mullamaa and Nikolayev, 1972]. With increasing depth the radiance varies to a lesser degree. It is noted that Tyler's [1960] instrument had a half angle of  $3.3^\circ$  and his prediction of the radiance variance is close to our estimations. We emphasize that the size of the refracted glitter pattern could impact the mean and variance of directional radiance. For example, an increasing wind speed and solar zenith angle will give a more diffuse pattern [Preisendorfer and Mobley, 1985], and as a consequence, the radiance will experience large variability in many directions. Under overcast skies, the wave effects are most pronounced near the extinction boundary of Snell's cone (Figure 3a).

[49] Based on Gordon and Ding [1992], a maximum self-shading error of 5% and 3% is found possible with the upwelling nadir radiance and upwelling plane irradiance data, respectively. Previous analyses of the full radiance distribution have been based on time-averaged fields made with multiple observations of radiance at fixed angles [e.g., Lundgren and Højerslev, 1971; Tyler, 1960]. Our data are however, limited to the near-surface light field, and have not reached the asymptotic radiance field [Preisendorfer, 1958]. The asymptotic light field has only been occasionally reported from previous field observations [e.g., Lundgren and Højerslev, 1971] which in theory is only achieved at optical depths greater than  $\sim 10$  [see Berwald et al., 1995; Højerslev and Zaneveld, 1977].

[50] The instrument calibrations and data validations suggest a combined uncertainty of less than 10% in the measured radiances. Since the imager sensor uses a non-linear responsivity function, the radiance at highest and lowest ends of the curve could be subject to larger errors. The discussions above have, however, included both the measurement uncertainties and the light field variability induced by environmental conditions.

[51] The errors in the radiance distribution propagate to the irradiance field as well, but to a smaller degree. The sensor tilts could also contribute to variability of apparent optical properties. The radiance distribution was corrected for tilts so that some pixels near the horizon were actually lost. The error resulting from this for computations of irradiance is small however, given the strong near zenith peak in the downwelling field. For example, an instrument tilt of  $10^\circ$  causes a maximum underestimation of irradiance and a maximum overestimation of average cosine by 5%, and a  $5^\circ$  tilt results in a negligible error. For the upwelling light field however, a  $5^\circ$  tilt could cause an error of 10% for the scalar irradiance and average cosine. Under overcast skies, the error would be higher since the intrascene dynamic range of the radiance distribution is lower and the radiance at large angles will take a more important role during integration.

[52] The accuracy of the absolute laboratory calibrations is evident by comparison with the traditional fixed channel downwelling irradiance sensor and upwelling radiance sensor (Figure 9) which show a slight bias and a high degree of correlation. Results are better for the direct comparison of upwelling radiances than the computed downwelling irradiances.

[53] The radiance distributions are used to calculate diffuse attenuation coefficients, as well as the average cosines. The average cosine for the downwelling light field shows a relationship with solar angle similar to that observed and described by *Aas and Højerslev* [1999]. The fitted line in Figure 7 deviates from the simple cosine model, which is suitable for collimated light only. *Aas and Højerslev* [1999] reported a similar trend for  $\bar{\mu}_d$  in the western Mediterranean. Their data were measured at wavelengths of 465–474 nm, which is much more diffuse than the wavelength used in our work (555 nm).

[54] To compare this result with the bidirectional reflectance model [*Morel et al.*, 2002], we derived a water column average chlorophyll concentration,  $\text{Chl} = 0.04 \text{ mg m}^{-3}$ , for the first optical depth ( $\sim 16.5 \text{ m}$  for light at 555 nm in Pacific region). *Morel's* model predicts a  $Q$  factor of  $3.42 \pm 0.21 \text{ sr}$ , nearly identical to our observation. *Zibordi and Berthon* [2001] suggest that the  $Q$  factor relates to the diffuse attenuation coefficient, and using their approach, we computed the  $Q$  factor of 4.84 sr for the Bedford Basin, which compares to our observation of 4.48 sr.

[55] The radiance distribution data have been combined with the Gershun's law to derive the absorption coefficient in clear waters [*Jerlov and Nygård*, 1968; *Lundgren and Højerslev*, 1971; *Voss*, 1989b]. Computation of the absorption coefficient in surface waters (Figure 8) exhibits discrepancies with direct measurements based on the ac-9 instrument. The "errors" could be from uncertainties of measurement and data processing as discussed above, but likely derive to large extent from missing source terms,

especially Raman scattering, in the radiative transfer equation [see *Voss*, 1989b]. On the other hand, there is usually a large amount of uncertainty associated with the direct measurement of absorption coefficient itself [*Leymarie et al.*, 2010]. For example, a significant source of error in the comparison of the inverse algorithms with direct measurement stems from the different spatial scales measured; Gershun's law predicts the bulk absorption coefficient over volumes of order  $1 \text{ m}^{-3}$ , while the in situ spectroradiometer like the ac-9 measures the optical properties for a very small volume of water, after it has been pumped into the instrument. All these issues together contribute to the uncertainties in the data-data comparison (Figure 10).

## 6. Summary

[56] We have obtained a complete description of the full radiance distribution in downwelling and upwelling hemispheres in a range of near-surface sea environments. Our data on the mean radiance field are consistent with previous investigations, but provide additional information on the dynamics and fine structure, particularly near the sea surface. The high-resolution observations allow better understanding of the measurement variability and the boundary conditions (e.g., the surface wavefield) and permit the validation of advanced radiative transfer models. The estimation of the full radiance field makes it possible to estimate other radiative quantities (e.g., irradiances) and the apparent optical properties in all three water bodies. A good agreement is obtained for the radiance measurements and data from other, more traditional sources. While the results shown here are based on depth profiles, a full understanding of the dynamics of the radiance field calls for analyses in the time domain, a topic for forthcoming studies.

## Notation

$L(\theta, \varphi)$	radiance, $\mu\text{Wcm}^{-2}\text{sr}^{-1}\text{nm}^{-1}$ .
$\theta$	zenith angle, degrees.
$\varphi$	azimuth angle, degrees.
$\Omega$	solid angle, sr.
$E_d$	downwelling plane irradiance, $\mu\text{Wcm}^{-2}\text{nm}^{-1}$ .
$E_u$	upwelling plane irradiance, $\mu\text{Wcm}^{-2}\text{nm}^{-1}$ .
$E_{od}$	downwelling scalar irradiance, $\mu\text{Wcm}^{-2}\text{nm}^{-1}$ .
$E_{ou}$	upwelling scalar irradiance, $\mu\text{Wcm}^{-2}\text{nm}^{-1}$ .
$E_{\text{net}}$	net irradiance, $E_{\text{net}} = E_d - E_u$ , $\mu\text{Wcm}^{-2}\text{nm}^{-1}$ .
$K_L$	diffuse attenuation coefficient for radiance, $\text{m}^{-1}$ .
$K_d, K_{od}$	diffuse attenuation coefficient for $E_d$ and $E_{od}$ , $\text{m}^{-1}$ .
$K_u, K_{ou}$	diffuse attenuation coefficient for $E_u$ and $E_{ou}$ , $\text{m}^{-1}$ .
$K_{\text{net}}$	diffuse attenuation coefficient for $E_{\text{net}}$ , $\text{m}^{-1}$ .
$\bar{\mu}_d, \bar{\mu}_u$	average cosine for downwelling and upwelling light field.
$\bar{\mu}$	average cosine for total light field.
$R$	irradiance reflectance, $R = E_u/E_d$ .
$a$	absorption coefficient, $\text{m}^{-1}$ .
$b$	scattering coefficient, $\text{m}^{-1}$ .
$c$	attenuation coefficient, $c = a + b$ , $\text{m}^{-1}$ .
$b_b$	backscattering coefficient, $\text{m}^{-1}$ .
$\beta$	volume scattering function, $\text{m}^{-1}\text{sr}^{-1}$ .
$\tilde{\beta}$	scattering phase function, $\tilde{\beta} = \beta/b$ , $\text{sr}^{-1}$ .
$L_u$	nadir radiance, $L(\theta = 180^\circ)$ , $\mu\text{Wcm}^{-2}\text{sr}^{-1}\text{nm}^{-1}$ .
$Q$	$Q$ factor, $Q = E_u/L_u$ , sr.

$\overline{\text{Chl}}$  average chlorophyll concentration,  $\text{mg m}^{-3}$ .  
 $\theta_s$  solar zenith angle, degrees.  
 $\alpha_{1/2}$  half angle of the radiance sensor, degrees.

[57] **Acknowledgments.** This work was sponsored by the Office of Naval Research under the Radiance in a Dynamic Ocean (RaDyO) program through contract N00014-09-C-0084 (MRL) and N00014-11-1-0153 (KJV). We are indebted to Michael Twardowski and Scott Freeman (WET Labs, Inc.) for sharing the ac-9 data in the Santa Barbara Channel and the Pacific Ocean. Our thanks also go to John Cullen (Dalhousie University, Halifax, Canada) who has kindly provided historical ac-9 data in the Bedford Basin, Nova Scotia. The authors are grateful to three anonymous reviewers for their comments and suggestions.

## References

- Aas, E., and N. K. Høgerslev (1999), Analysis of underwater radiance observations: Apparent optical properties and analytic functions describing the angular radiance distribution, *J. Geophys. Res.*, *104*, 8015–8024, doi:10.1029/1998JC900088.
- Adams, J. T., E. Aas, N. K. Høgerslev, and B. Lundgren (2002), Comparison of radiance and polarization values observed in the Mediterranean Sea and simulated in a Monte Carlo model, *Appl. Opt.*, *41*, 2724–2733, doi:10.1364/AO.41.002724.
- Anderson, C. R., D. A. Siegel, M. A. Brzezinski, and N. Guillocheau (2008), Controls on temporal patterns in phytoplankton community structure in the Santa Barbara Channel, California, *J. Geophys. Res.*, *113*, C04038, doi:10.1029/2007JC004321.
- Berwald, J., D. Stramski, C. D. Mobley, and D. A. Kiefer (1995), Influences of absorption and scattering on vertical changes in the average cosine of the underwater light field, *Limnol. Oceanogr.*, *40*, 1347–1357, doi:10.4319/lo.1995.40.8.1347.
- Chami, M., E. B. Shybanov, G. A. Khomenko, M. E.-G. Lee, O. V. Martynov, and G. K. Korotaev (2006), Spectral variation of the volume scattering function measured over the full range of scattering angles in a coastal environment, *Appl. Opt.*, *45*, 3605–3619, doi:10.1364/AO.45.003605.
- Chang, G. C., A. H. Barnard, S. McLean, P. J. Egli, C. Moore, J. R. V. Zaneveld, T. D. Dickey, and A. Hanson (2006), In situ optical variability and relationships in the Santa Barbara Channel: Implications for remote sensing, *Appl. Opt.*, *45*, 3593–3604, doi:10.1364/AO.45.003593.
- Collins, D. G., W. G. Blättner, M. B. Wells, and H. G. Horak (1972), Backward Monte Carlo calculations of the polarization characteristics of the radiation emerging from spherical-shell atmospheres, *Appl. Opt.*, *11*, 2684–2696, doi:10.1364/AO.11.002684.
- Cox, C., and W. Munk (1954), Statistics of the sea surface derived from sun glitter, *J. Mar. Res.*, *13*, 198–227.
- Cox, C., and W. Munk (1956), Slopes of the sea surface deduced from photographs of sun glitter, *Bull. Scripps Inst. Oceanogr.*, *6*, 401–488.
- Gershun, A. A. (1939), The light field [English translation, P. Moon and G. Timoshenko], *J. Math Phys. Cambridge Mass.*, *18*, 51–151.
- Gordon, H. R., and K. Ding (1992), Self-shading of in-water optical instruments, *Limnol. Oceanogr.*, *37*, 491–500, doi:10.4319/lo.1992.37.3.0491.
- Hirata, T. (2003), Irradiance inversion theory to retrieve volume scattering function of seawater, *Appl. Opt.*, *42*, 1564–1573, doi:10.1364/AO.42.001564.
- Hirata, T., and N. K. Høgerslev (2008), Relationship between the irradiance reflectance and inherent optical properties of seawater, *J. Geophys. Res.*, *113*, C03030, doi:10.1029/2007JC004325.
- Hirata, T., N. Hardman-Mountford, J. Aiken, and J. Fishwick (2009), Relationship between the distribution function of ocean nadir radiance and inherent optical properties for oceanic waters, *Appl. Opt.*, *48*, 3129–3138, doi:10.1364/AO.48.003129.
- Høgerslev, N. K. (1994), A history of early optical oceanographic instrument design in Scandinavia, in *Ocean Optics*, edited by R. W. Spinrad et al., pp. 118–147, Oxford Univ. Press, New York.
- Høgerslev, N. K., and J. R. Zaneveld (1977), A theoretical proof of the existence of the submarine asymptotic daylight field, *Rep. 34*, 16 pp., Dep. of Phys. Oceanogr., Univ. of Copenhagen, Copenhagen.
- Hubbard, B. E. et al. (2006), The virtual periscope, paper presented at Ocean Optics XVIII, Oceanogr. Soc., Montreal, Que., Canada, 9–13 Oct.
- Jerlov, N. G. (1976), *Marine Optics*, 231 pp., Elsevier Sci., Amsterdam.
- Jerlov, N. G., and M. Fukuda (1960), Radiance distribution in the upper layers of the sea, *Tellus*, *12*, 348–355, doi:10.1111/j.2153-3490.1960.tb01319.x.
- Jerlov, N. G., and K. Nygård (1968), Inherent optical properties computed from radiance measurements in the Baltic, *Rep. 1*, 6 pp., Inst. for Phys. Oceanogr., Copenhagen.
- Kirk, J. T. O. (1994), *Light and Photosynthesis in Aquatic Ecosystems*, 2nd ed., 509 pp., Cambridge Univ. Press, New York, doi:10.1017/CBO9780511623370.
- Leymarie, E., et al. (2010), Uncertainties associated to measurements of inherent optical properties in natural waters, *Appl. Opt.*, *49*, 5415–5436, doi:10.1364/AO.49.005415.
- Lundgren, B., and N. K. Høgerslev (1971), Daylight measurements in the Sargasso Sea: Results from the “Dana” expedition (January–April 1966), *Rep. 14*, 44 pp., Dep. of Phys. Oceanogr., Univ. of Copenhagen, Copenhagen.
- Mobley, C. D. (1989), A numerical model for the computation of radiance distributions in natural waters with wind-roughened surfaces, *Limnol. Oceanogr.*, *34*, 1473–1483, doi:10.4319/lo.1989.34.8.1473.
- Mobley, C. D. (1994), *Light and Water: Radiative Transfer in Natural Waters*, 592 pp., Academic, San Diego, Calif.
- Mobley, C. D., B. Gentili, H. R. Gordon, Z. Jin, G. W. Kattawar, A. Morel, P. Reinersman, K. Stamnes, and R. H. Stavn (1993), Comparison of numerical models for computing underwater light fields, *Appl. Opt.*, *32*, 7484–7504, doi:10.1364/AO.32.007484.
- Morel, A. (1974), Optical properties of pure water and pure sea water, in *Optical Aspects of Oceanography*, edited by N. G. Jerlov and E. Steemann Nielsen, pp. 1–24, Academic, New York.
- Morel, A. (1991), Light and marine photosynthesis: A spectral model with geochemical and climatological implications, *Prog. Oceanogr.*, *26*, 263–306, doi:10.1016/0079-6611(91)90004-6.
- Morel, A., and B. Gentili (1993), Diffuse reflectance of oceanic waters. Part II. Bidirectional aspects, *Appl. Opt.*, *32*, 6864–6879, doi:10.1364/AO.32.006864.
- Morel, A., K. J. Voss, and B. Gentili (1995), Bidirectional reflectance of oceanic waters: A comparison of model and measured upward radiance fields, *J. Geophys. Res.*, *100*, 13,143–13,150, doi:10.1029/95JC00531.
- Morel, A., D. Antoine, and B. Gentili (2002), Bidirectional reflectance of oceanic waters: Accounting for Raman scattering and varying particle scattering phase function, *Appl. Opt.*, *41*, 6289–6306, doi:10.1364/AO.41.006289.
- Mueller, J. L., and R. W. Austin (1995), *Ocean Optics Protocols for SeaWiFS Validation, Revision 1*, *SeaWiFS Tech. Rep. Ser.*, vol. 25, 66 pp., NASA, Greenbelt, Md.
- Mullamaa, Y.-A. R., and V. P. Nikolayev (1972), Fluctuations of the luminance of the sun as measured under water, *Izv. Russ. Acad. Sci. Atmos. Oceanic Phys.*, *8*, 382–388.
- Preisendorfer, R. W. (1958), Some practical consequences of the asymptotic radiance hypothesis, *SIO Ref. Ser.*, *58–60*, 1–31.
- Preisendorfer, R. W. (1959), Theoretical proof of the existence of characteristic diffuse light in natural waters, *J. Mar. Res.*, *18*, 1–9.
- Preisendorfer, R. W. (1976), *Hydrologic Optics*, 218 pp., Natl. Oceanic and Atmos. Organ., Honolulu.
- Preisendorfer, R. W., and C. D. Mobley (1985), Unpolarized irradiance reflectances and glitter patterns of random capillary waves on lakes and seas, by Monte Carlo simulation, *NOAA Tech. Memo. ERL PMEL-63*, 145 pp., Pac. Mar. Environ. Lab., Seattle, Wash.
- Reda, I., and A. Andreas (2004), Solar position algorithm for solar radiation applications, *Sol. Energy*, *76*, 577–589, doi:10.1016/j.solener.2003.12.003.
- Sasaki, T., S. Watanabe, G. Oshiba, and N. Okami (1958), Measurements of angular distribution of submarine daylight by means of a new instrument, *J. Oceanogr. Soc. Jpn.*, *14*, 47–52.
- Smith, R. C. (1974), Structure of solar radiation in the upper layers of the sea, in *Optical Aspects of Oceanography*, edited by N. G. Jerlov and E. Steemann Nielsen, pp. 95–119, Academic, London.
- Smith, R. C., R. W. Austin, and J. E. Tyler (1970), An oceanographic radiance distribution camera system, *Appl. Opt.*, *9*, 2015–2016, doi:10.1364/AO.9.002015.
- Strain, P. M., and P. A. Yeats (1999), The relationships between chemical measures and potential predictors of the eutrophication status of inlets, *Mar. Pollut. Bull.*, *38*, 1163–1170, doi:10.1016/S0025-326X(99)00151-4.
- Stramski, D., and J. Dera (1988), On the mechanism for producing flashing light under a wind-disturbed water surface, *Oceanologia*, *25*, 5–21.
- Tyler, J. E. (1960), Radiance distribution as a function of depth in an underwater environment, *Bull. Scripps Inst. Oceanogr.*, *7*, 363–411.
- Van Dommelen, R. et al. (2010), Instrumentation, calibration and validation of a high dynamic range radiance camera, paper presented at Ocean Optics XX, Oceanogr. Soc., Anchorage, Alaska, 27 Sept. to 1 Oct.
- Voss, K. J. (1989a), Electro-optic camera system for measurement of the underwater radiance distribution, *Opt. Eng.*, *28*, 384–387.
- Voss, K. J. (1989b), Use of the radiance distribution to measure the optical absorption coefficient in the ocean, *Limnol. Oceanogr.*, *34*, 1614–1622, doi:10.4319/lo.1989.34.8.1614.

- Voss, K. J., and A. L. Chapin (1992), Next generation in-water radiance distribution camera system, paper presented at Ocean Optics XI, Soc. of Photo-Opt. Instrum. Eng., San Diego, Calif., 20–22 Jul.
- Voss, K., and A. Chapin (2005), Upwelling radiance distribution camera system, NURADS, *Opt. Express*, *13*, 4250–4262, doi:10.1364/OPEX.13.004250.
- Voss, K. J., and A. Morel (2005), Bidirectional reflectance function for oceanic waters with varying chlorophyll concentrations: Measurements versus predictions, *Limnol. Oceanogr.*, *50*, 698–705, doi:10.4319/lo.2005.50.2.0698.
- Voss, K. J., and G. Zibordi (1989), Radiometric and geometric calibration of a visible spectral electro-optic fisheye camera radiance distribution system, *J. Atmos. Oceanic Technol.*, *6*, 652–662, doi:10.1175/1520-0426(1989)006<0652:RAGCOA>2.0.CO;2.
- Voss, K. J., C. D. Mobley, L. K. Sundman, J. E. Ivey, and C. H. Mazel (2003), The spectral upwelling radiance distribution in optically shallow waters, *Limnol. Oceanogr.*, *48*, 364–373, doi:10.4319/lo.2003.48.1\_part.2.0364.
- Voss, K. J., A. A. Morel, and D. Antoine (2007), Detailed validation of the bidirectional effect in various Case 1 waters for application to ocean color imagery, *Biogeosciences*, *4*, 781–789, doi:10.5194/bg-4-781-2007.
- Voss, K. J. et al. (2010), An example crossover experiment for testing new vicarious calibration techniques for satellite ocean color radioemetry, *J. Atmos. Oceanic Technol.*, *27*, 1747–1759, doi:10.1175/2010JTECHO737.1.
- Waters, K. J., R. C. Smith, and M. R. Lewis (1990), Avoiding ship-induced light-field perturbation in the determination of oceanic optical properties, *Oceanography*, *3*, 18–21.
- Wei, J. et al. (2010), Radiance distribution as a function of depth in sea water, paper presented at Ocean Optics XX, Oceanogr. Soc., Anchorage, Alaska, 27 Sept. to 1 Oct.
- Zaneveld, J. R. V., and H. Pak (1972), Some aspects of the axially symmetric submarine daylight field, *J. Geophys. Res.*, *77*, 2677–2680, doi:10.1029/JC077i015p02677.
- Zaneveld, J. R. V., E. Boss, and A. Barnard (2001a), Influence of surface waves on measured and modeled irradiance profiles, *Appl. Opt.*, *40*, 1442–1449, doi:10.1364/AO.40.001442.
- Zaneveld, J. R. V., E. Boss, and P. Hwang (2001b), The influence of coherent waves on the remotely sensed reflectance, *Opt. Express*, *9*, 260–266, doi:10.1364/OE.9.000260.
- Zhang, X., M. Twardowski, and M. Lewis (2011), Retrieving composition and sizes of oceanic particle subpopulations from the volume scattering function, *Appl. Opt.*, *50*, 1240–1259, doi:10.1364/AO.50.001240.
- Zibordi, G., and J. F. Berthon (2001), Relationships between Q-factor and seawater optical properties in a coastal region, *Limnol. Oceanogr.*, *46*, 1130–1140, doi:10.4319/lo.2001.46.5.1130.

---

M. R. Lewis and J. Wei, Department of Oceanography, Dalhousie University, 1355 Oxford St., Halifax, NS B3H 4R2, Canada. (marlon.lewis@dal.ca)

R. Van Dommelen, Satlantic, Inc., 3481 N. Marginal Rd., Pier 9, Richmond Terminals, Halifax, NS B3K 5X8, Canada.

K. J. Voss, Department of Physics, University of Miami, Coral Gables, FL 33124, USA.